

A Comparison of Electronic, Dielectric, and Thermoelectric Properties of Monolayer of HfX_2N_4 ($X = \text{Si}, \text{Ge}$) through First-Principles Calculations

Chayan Das ^a, Abhishek ^b, Dibyajyoti Saikia ^a, Appala Naidu Gandhi ^b, Satyajit Sahu

^{a*}

^a *Department of Physics, Indian Institute of Technology Jodhpur, Jodhpur 342037, India*

^b *Department of Metallurgical and Materials Engineering, Indian Institute of Technology Jodhpur, Jodhpur 342037, India*

Abstract

The newly emerged two-dimensional (2D) materials family of MSi_2N_4 , where M is a transition metal atom (i.e., Mo, W, etc.), has the potential to be named after the conventional and very popular transition metal di-chalcogenides (TMDC), which got their reputation for having bandgap tunability and high mobility. The HfSi_2N_4 and HfGe_2N_4 2D materials are members of the MSi_2N_4 family and possess very good figure of merit (ZT) and have high mobility, proving their suitability for thermoelectric applications. The HfSi_2N_4 and HfGe_2N_4 showed considerable ZT of 0.90 and 0.89, respectively, for p-type and 0.83 and 0.79 for n-type, at 900 K along with high mobility according to the solutions obtained after solving the Boltzmann Transport Equation (BTE). The HfGe_2N_4 also showed a ZT of 0.84 at 600 K and 0.68 at 300 K, which is also excellent for low-temperature operation. The bandgaps (BG) obtained for HfSi_2N_4 and HfGe_2N_4 according to the Heyd-Scuseria-Ernzerhof (HSE) approximation were 2.89 eV and 2.75 eV. The first absorption peak showed in the blue region of the visible spectrum; from this, their usefulness in visible range photodetectors can also be inferred.

1. Introduction

The extraordinary electrical¹, thermal², and optical² properties exhibited by two-dimensional (2D) materials have been witnessed in recent times, which attracted considerable interest in exploring more of these materials³⁻⁶. MoSi₂N₄ monolayer (ML), a member of the MX₂N₄ family, was recently synthesized using the CVD method on a centimeter scale⁷ with high strength and stability⁸, which motivates researchers to explore more in this direction. Thermoelectrics can be used for the efficient utilization of energy resources. As non-renewable energy sources are depleting, people need to think more and more about efficient utilization of existing resources. In this work, Boltzmann transport theory along with the first-principles calculations were considered to evaluate the 2D MLs of HfSi₂N₄ and HfGe₂N₄. We obtained considerable Seebeck coefficients (S) and ZT . Here, ZT is the figure of merit, while the Seebeck coefficient quantifies the voltage produced when a gradient of temperature is used at the two extreme points of the material. An ideal thermoelectric material should have a combination of high electrical conductivity (σ) and S , as well as a low thermal conductivity ($k = k_e + k_l$). The overall thermal conductivity is affected by its two components, i.e., originating from electrons (k_e) and originating from (phonons) lattice (k_l). The 2D MLs exhibit exceptional stability, superior mobility, and favorable optoelectronic characteristics⁸. The crystal structure can be viewed as a metal atom (M) sandwiched between two nitrogen (N) atoms, and the whole section was again sandwiched between two buckled honeycomb XN layers where X = Si or Ge. Here M is the transition metal atom (Mo, W, Cr, Hf, etc.). One possible method for their synthesis is chemical vapor deposition (CVD). Recently, MoSi₂N₄ was synthesized by Yi-Lun and his coworkers by using CVD⁷. The mobility values of MoSi₂N₄ were predicted to be 490 cm²V⁻¹s⁻¹ and 2190 cm²V⁻¹s⁻¹ for n and p-type and for WSi₂N₄ the values were 668 cm²V⁻¹s⁻¹ and 1385 cm²V⁻¹s⁻¹ for n and p-type semiconductors^{8,9}. Considerable investigation has also been conducted on two-dimensional transition metal chalcogenide materials. The MoSe₂ ML was reported with an exceptionally low ZT of 0.2 and a high k_l of 60 Wm⁻¹K⁻¹. Qing Tan and his coworkers experimentally reported a low k_l of 1.25 Wm⁻¹K⁻¹ with SnS ML; however, the ZT value was found to be about 0.6 at 900 K¹⁰. TiS₂ ML was reported with a k_l of more than 4 Wm⁻¹K⁻¹ with ZT value of 0.5¹¹. WS₂ ML showed a very high k_l of 23.15 Wm⁻¹K⁻¹ along with a ZT of 0.66 at 900 K¹². HfS₂ ML showed a low k_l of 2.83 Wm⁻¹K⁻¹ with a considerable ZT of 0.90¹³. ZrOS Janus ML was also reported with a ZT of 0.82 with a very low k_l of 1.5 Wm⁻¹K⁻¹¹⁴. Apart from the 2D transition metal chalcogenides, MoSi₂N₄, and MoGe₂N₄, were

reported with a ZT of 0.42 and 0.94 along with k_l of $260 \text{ Wm}^{-1}\text{K}^{-1}$ and $80 \text{ Wm}^{-1}\text{K}^{-1}$ ¹⁵. WSi_2N_4 and WGe_2N_4 were also reported with a ZT of 0.72 and 0.91, along with a k_l of $114.9 \text{ Wm}^{-1}\text{K}^{-1}$ and $9.41 \text{ Wm}^{-1}\text{K}^{-1}$ ⁹. Research is still going on with the new 2D materials to improve their performance as thermoelectric materials. Here, we studied the electrical, optical, and thermoelectric properties of HfSi_2N_4 and HfGe_2N_4 using the first-principles calculations associated with DFT and BTE. The HfGe_2N_4 ML exhibited an excellent ZT of 0.90 (0.83 for n-type), which is better in comparison to HfSi_2N_4 , which exhibited a ZT of 0.89 (0.79 for n-type) at 900 K for p-type doping. So, a strategic comparison of thermoelectric and optical properties is needed to understand the physical and chemical properties, which play an important role in the difference in their properties. The HfSi_2N_4 and HfGe_2N_4 possess similar bandgaps. As a result, they show absorption peaks in the same wavelength range, which was blue in the visible range, i.e. 490 nm and 493 nm, respectively.

2. Methodology

First-principles calculations were performed with the projector augmented wave (PAW)^{16,17} method implemented in Vienna ab-initio Simulation Package (VASP)¹⁸ with exchange-correlation interaction of Perdew-Burke-Ernzerhof (PBE) functionals¹⁹. The DFT-D3 method of Grimme was used to include the van der Waals (vdW) interactions. A vacuum of 30 Å thickness was maintained along the z-direction to avoid the interaction of two layers. The geometry optimization was performed using a gamma (Γ) centered $12 \times 12 \times 1$ k-meshes. The energy cutoff was set to 520 eV, and the electronic and ionic convergence criteria were set to 10^{-6} eV and 10^{-5} eV/Å. The phonon band structure was obtained from the Phonopy package in combination with VASP using $2 \times 2 \times 1$ supercells with forces estimated employing Γ centered $9 \times 9 \times 1$ k-meshes. More accurate representation of the electronic band structure is obtained employing the Heyd-Scuseria-Ernzerhof (HSE) hybrid functionals²⁰. $15 \times 15 \times 1$ k-meshes were utilized, along with the previously determined ionic, electronic convergence and kinetic energy cutoffs levels. The ab initio molecular dynamics (AIMD) calculation, mobility, and relaxation time calculations were performed using the Quantum Espresso (QE) Package^{21,22}. In these calculations, $15 \times 15 \times 1$ k-meshes were used for the Brillouin zone integrations and an energy cutoff value of 50 Ry was used for the electronic wave functions. 10^{-9} Ry was used as electronic energy convergence criterion in these calculations. The optical response as a function of frequency was evaluated using the Bethe-Salpeter equation (BSE) [8]. In these hybrid BSE (HSE+BSE) calculations the $9 \times 9 \times 1$ Γ centred k-meshes were used.

The many-body perturbation theory calculation necessitates a significant number of unoccupied states. As a result, 128 electronic bands were taken into account. The refractive index (η) and extinction coefficient (K) were determined using the following formulae.

$$\eta = \left[\frac{\{(\varepsilon_r^2 + \varepsilon_i^2)^{1/2} + \varepsilon_r\}}{2} \right]^{1/2} \quad (1)$$

$$K = \left[\frac{\{(\varepsilon_r^2 + \varepsilon_i^2)^{1/2} - \varepsilon_r\}}{2} \right]^{1/2} \quad (2)$$

And using them, the absorption coefficient (α) was also determined.

$$\alpha = \frac{2K\omega}{c} \quad (3)$$

Here, ε_r , ε_i are real and imaginary parts of the dielectric function, and ω , and C are frequency, and speed of light, respectively. Thermoelectric transport coefficients i.e. Seebeck coefficient ($S_{l,m}$), electrical conductivity ($\sigma_{l,m}$), and electronic thermal conductivity ($k_{l,m}$) were obtained from the semi-classical BTE with the constant scattering time approximation (CRTA) implemented in BoltzTraP code ²³.

$$\sigma_{l,m} = \frac{1}{\Omega} f \sigma_{l,m}(\varepsilon) \left[-\frac{\Delta f_{\phi}(T,\varepsilon)}{\Delta \varepsilon} \right] d\varepsilon \quad (4)$$

$$k_{l,m}(T, \phi) = \frac{1}{e^2 T \Omega} f \sigma_{l,m}(\varepsilon) (\varepsilon - \phi)^2 \left[-\frac{\Delta f_{\phi}(T,\varepsilon)}{\Delta \varepsilon} \right] d\varepsilon \quad (5)$$

$$S_{l,m}(T, \phi) = \frac{(\sigma^{-1})_{n,l}}{eT\Omega} f \sigma_{n,m}(\varepsilon) (\varepsilon - \phi) \left[-\frac{\Delta f_{\phi}(T,\varepsilon)}{\Delta \varepsilon} \right] d\varepsilon \quad (6)$$

Here, e , ϕ , Ω , T are the electron charge, chemical potential, unit cell volume, and temperature, respectively. Lattice contribution to the thermal conductivity (k_l) is calculated using the phono3py package in combination with quantum espresso by evaluating the third-order force constants with the finite displacement (0.06 Å) method. In phono3py, a $2 \times 2 \times 1$ supercell was used, and the forces were estimated employing $9 \times 9 \times 1$ k-meshes.

3. Result and Discussion

3.1. Structure and Stability

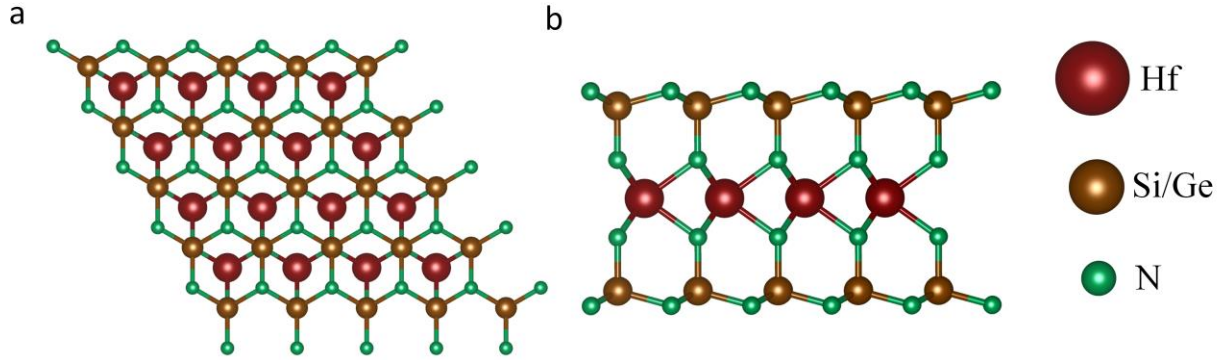


Figure 1: Visualization of (a) top and (b) side view of HfX_2N_4 ($X = \text{Si}, \text{Ge}$) ML with $4 \times 4 \times 1$ supercell.

The HfX_2N_4 ML, where X can be Si or Ge, can be seen as a ML of HfN_2 positioned between two honeycomb layers made of SiN or GeN. The three layers are arranged in a stacked formation. The Hf atom is located in the center of a trigonal prism structure composed of six Si atoms. The HfN_2 layer is linked to the (SiN/GeN) layers via vertically aligned Si-N connections (**Figure 1(a)**). HfX_2N_4 possesses a hexagonal structure (**Figure 1(b)**), which belongs to the space groups of $P\text{-}6m2$ (No. 187) ⁸. The optimized lattice constant values for HfSi_2N_4 were consistent with prior findings ⁸. The lattice constants for HfGe_2N_4 were also optimized. **Table 1** represents the summary of optimized lattice constants (a), thickness (t), bond lengths (d), and angles (θ) for the two MLs. It was observed that the bond length in the HfGe_2N_4 is greater compared to that of HfSi_2N_4 as the atomic radius of Ge is greater than the atomic radius of Si.

Table 1: Calculated lattice constants (a), thickness (t), bond lengths (d), and angles (θ) for 2D ML of HfSi_2N_4 and HfGe_2N_4 .

Monolayer	$a(=b)$ (Å)	Thickness (Å)	$d(\text{Hf-N})$ (Å)	$d(\text{X-N})$ (Å)	$\theta(\text{Hf-N-Hf})$	$\theta(\text{N-X-N})$	$\theta(\text{Hf-N-X})$
HfSi_2N_4	3.01	11.36	2.14	1.75	71.57	105.58	125.78
HfGe_2N_4	3.14	11.50	2.18	1.90	67.33	108.86	123.66

Cohesive energy provides insight into the structural stability of a material. The cohesive energy (E_{co}) was determined using the provided formula: $E_{co} = \{(E_{Hf} + 2 \times E_X + 4 \times E_N) - E_{HfX_2N_4}\} / 7$. The $E_{HfX_2N_4}$ is the energy of HfX_2N_4 ML and E_{Hf} , E_X , and E_N are the atomic energy of single Hf, X, and N, respectively. The obtained E_{co} per atom was evaluated as 1.11 eV and 0.50 eV for $HfSi_2N_4$ and $HfGe_2N_4$ MLs indicating their thermodynamic stability. We assessed the dynamical stability of $HfSi_2N_4$ and $HfGe_2N_4$ by calculating their phonon dispersion curves along the Γ -M-K- Γ path and shown in **Figure 2**. No imaginary frequencies in the phonon band structures reaffirms the thermodynamic stability of these structures. The maximum phonon frequency found in $HfSi_2N_4$ and $HfGe_2N_4$ were 29.89 THz and 26.00 THz, respectively, suggesting that the $HfGe_2N_4$ has a lower maximum frequency compared to $HfSi_2N_4$. Twenty-one different vibrational modes were found as the ML's unit cells contain seven atoms. The first three modes from the bottom are called the acoustic modes, while the following eighteen modes are optical modes. The acoustic vibrational modes are in-plane longitudinal acoustic (LA) mode, transverse acoustic (TA) mode, and out-of-plane mode (ZA) from the bottom. The optical bands in the $HfGe_2N_4$ ML were found to overlap with the acoustic modes, in contrast to the $HfSi_2N_4$ ML, where the acoustic bands are separate. From the phonon density of states (PhDOS), it was found that the Hf atom contributed more towards acoustic modes compared to optical modes, and Si/Ge and N contributed more to the optical modes compared to acoustic modes. To ensure the practical applicability of a thermoelectric device operating at a high temperature of 900 K, we performed the ab initio molecular dynamics (MD) simulation for more than 4500 femtoseconds for both $HfSi_2N_4$ and $HfGe_2N_4$ under a micro-canonical ensemble at a temperature of 900 K. **Figures 2c and 2d** show the thermal stability of these two systems at 900 K.

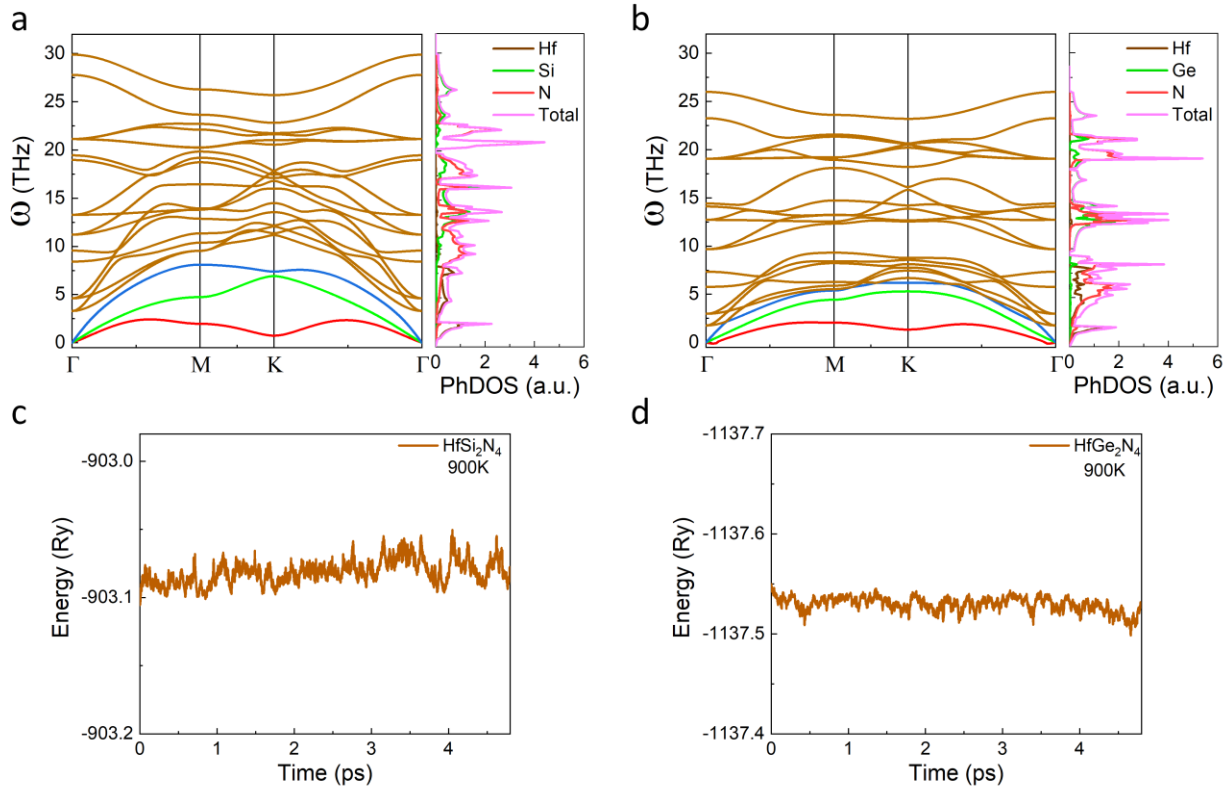


Figure 2: Calculated phonon band structure and phonon density of states in a) HfSi_2N_4 and b) HfGe_2N_4 ML. The red, green, and blue colored bands represent the ZA, TA, and LA modes, respectively. Energy fluctuation at 900 K estimated in MD simulations are shown in c) HfSi_2N_4 and d) HfGe_2N_4 .

3.2. Electronic Properties

Figures 3a and 3b show the electronic band structure from -4 eV to 4 eV of energy range. The calculation was performed along the Γ -M-K- Γ path for the HfSi_2N_4 and HfGe_2N_4 ML. The obtained BGs are 1.79 eV and 1.70 eV, respectively, for HfSi_2N_4 and HfGe_2N_4 according to PBE approximation. **Figures 3c and 3d** show the more accurate band structure of HfSi_2N_4 and HfGe_2N_4 obtained using hybrid functionals (HSE06), and the corresponding BG values are 2.89 eV and 2.75 eV, respectively. The BG values achieved for both materials match well with the values suggested by calculations conducted by Yadav et al.²⁴. The nature of both the band structures is indirect, and both the MLs show the conduction band minima (CBM) between Γ and M point. The valance band maximum (VBM) is between the M and K points in the case of HfSi_2N_4 . However, in the case of

HfGe₂N₄, the VBM is situated between the K and Γ points. From the DOS and local density of states (LDOS) obtained for the different elements, it was observed that for both the HfSi₂N₄ and HfGe₂N₄ MLs, the VBM is primarily contributed by the *p* orbitals of N atoms and *d* orbitals of Hf atoms. But CBM is primarily contributed by *d* of Hf atoms. It has been noted that in both the MLs, the element N has a more significant impact on the valence band, while Hf has a greater effect on the conduction band. The *p* orbital of Silicon (Si) and Germanium (Ge) make similar contributions to both the valence bands and conduction bands. Improved DOS calculations utilizing hybrid functionals (HSE06) exhibited a similar trend as those estimated using PBE functionals.

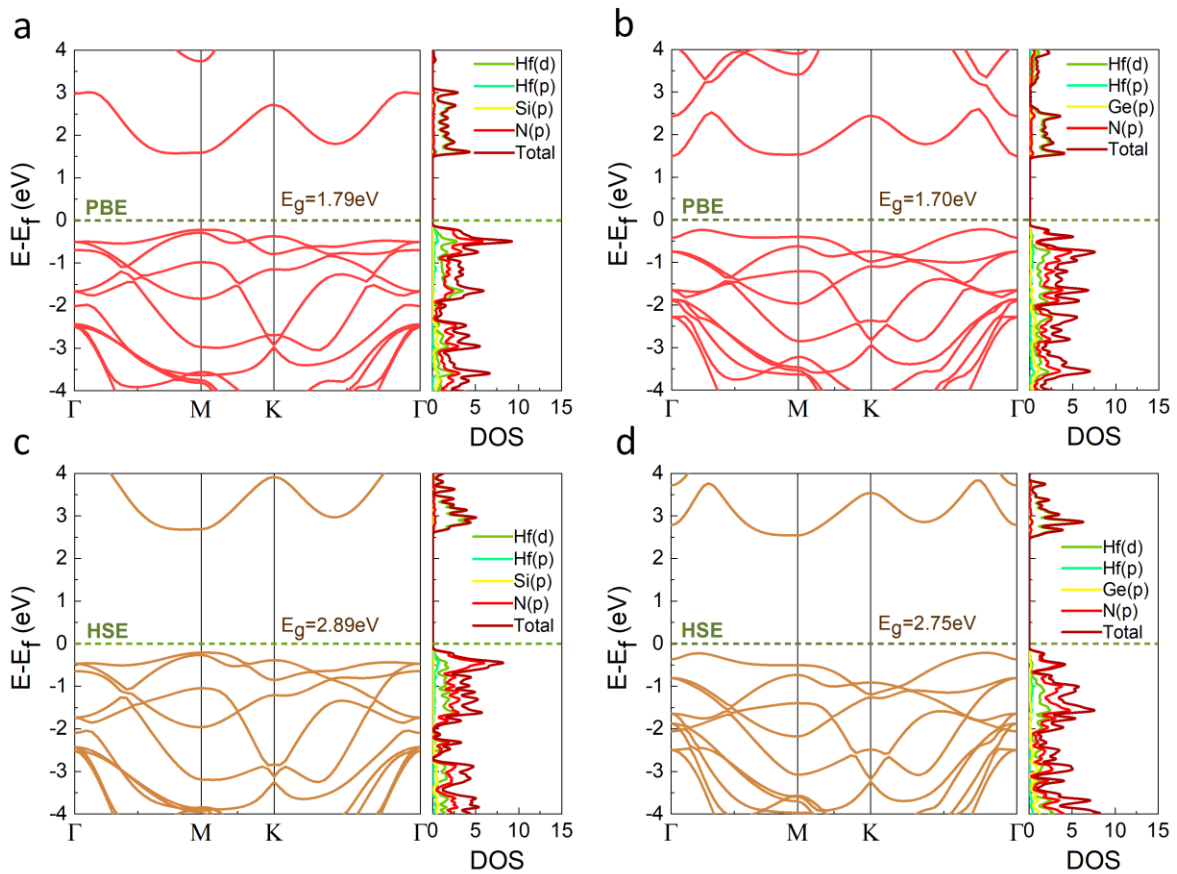


Figure 3: Calculated band structure and local density of states of the a) HfSi₂N₄ and b) HfGe₂N₄ MLs, obtained from PBE functionals, and c) HfSi₂N₄ and d) HfGe₂N₄ obtained from the HSE06 functionals.

3.3. Mobility and relaxation time

Bardeen and Shockley's deformation potential theory was used to calculate the mobility of electrons and holes according to PBE with QE. Here, the band shift was considered with changing strain, which was stated as the deformation potential of individual crystals²⁵. The individual mobilities of individual 2D systems can be determined by calculating the deformation potentials and taking into account the effective mass theorem, which is expressed as

$$\mu_{2D} = \frac{e\hbar^3 C_{2D}}{K_B T m_e^* m_a (E_I^2)} \quad (7)$$

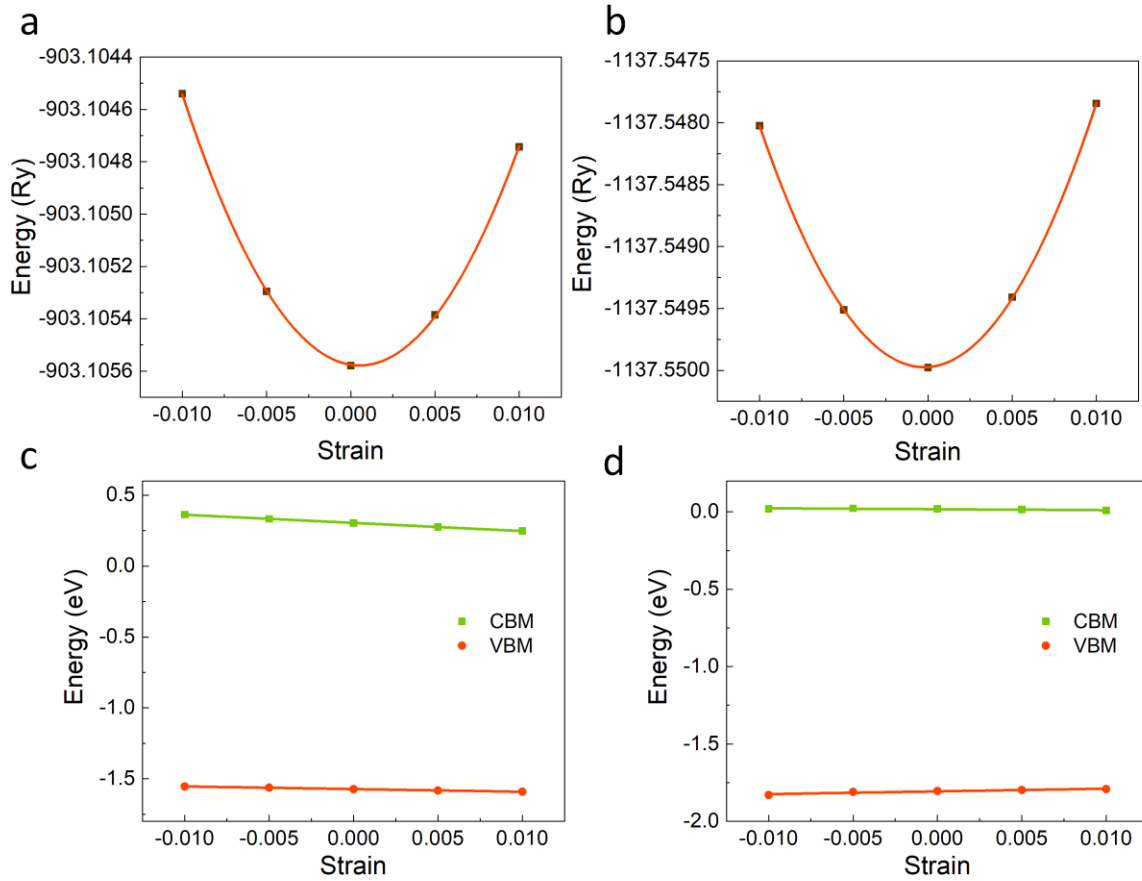


Figure 4: Variation of total energy with respect to uniaxial strain in a) HfSi₂N₄ and b) HfGe₂N₄. To determine the deformation potential, the VBM and CBM shift in c) HfSi₂N₄ and d) HfGe₂N₄ with respect to uniaxial strain has been calculated.

The elastic constant of 2D MLs is represented by C_{2D} of HfSi₂N₄ and HfGe₂N₄. We can derive this from the following formula $C_{2D} = (\frac{\partial^2 E}{\partial \epsilon^2} / A_0)$. We plot the energy values for different uniaxial strains and fit a parabola to determine C_{2D} from the plot of HfSi₂N₄ (**Figure 4a**) and for HfGe₂N₄

(Figure 4b). Here A_0 represents the area of the individual MLs in the absence of strain, T denotes the temperature in Kelvin, K_B represents the Boltzmann constant, and m^* signifies the effective mass, which is estimated using $m^* (= \frac{1}{\hbar^2} \frac{d^2E}{dk^2})$ for electron and holes, and $m_a = \sqrt{m_x^* m_y^*}$ is the geometric average of in-plane effective masses. As the effective mass also possesses a second-order derivative, we can get it from the band edge of VBM (for hole) and CBM (for electron) by fitting a parabola. The obtained C_{2D} is 388.08 Nm^{-1} , and hole mobility (μ_h) is $582.35 \text{ cm}^2\text{V}^{-1}\text{s}^{-1}$ for HfSi_2N_4 . The C_{2D} and μ_h of HfGe_2N_4 were calculated to be 330.71 Nm^{-1} and $1870.08 \text{ cm}^2\text{V}^{-1}\text{s}^{-1}$, and are in agreement with the previous results^{8,26}. The deformation potential ($E_I = \frac{\partial V}{\partial \varepsilon}$), was calculated from the change in band edges (V) with the application of strain (ε). Figures 4(c) and (d) represent the change of CBM and VBM band edges for HfSi_2N_4 and HfGe_2N_4 . Relaxation time (τ) for electrons and holes for HfSi_2N_4 and HfGe_2N_4 can be evaluated from the following expression: $\tau = \frac{\mu m^*}{e}$. The complete set of parameters acquired for both structures is presented in Table 2, and m_0 represents the rest mass of the electron. The materials of our interest show very high mobility (μ), which exceeds the mobility of many reported 2D materials by more than ten times, i.e., MoS_2 ($72 \text{ cm}^2\text{V}^{-1}\text{s}^{-1}$) and WS_2 ($21 \text{ cm}^2\text{V}^{-1}\text{s}^{-1}$)²⁷. The μ of these materials is similar to that of boron phosphorous (BP) and boron arsenide (BAs); however, they are unsuitable for thermoelectric applications due to their exceedingly high κ_l of approximately $4 \times 10^2 \text{ W/mK}$ ²⁸.

Table 2: Calculated C_{2D} , E_I , m^* , μ , and τ of ML of HfSi_2N_4 and HfGe_2N_4 for both electrons and holes according to PBE.

Crystal	C_{2D} (N/m)	$E_{I,(electron)}$ (eV)	$E_{I,(hole)}$ (eV)	m_e^* / m_0	m_h^* / m_0	μ_e ($\text{cm}^2\text{V}^{-1}\text{s}^{-1}$)	μ_h ($\text{cm}^2\text{V}^{-1}\text{s}^{-1}$)	τ_e (s) × 10^{-13}	τ_h (s) × 10^{-13}
HfSi_2N_4	388.08	5.78	1.87	1.16	2.017	181.20	582.35	1.20	6.68
HfGe_2N_4	330.71	4.39	1.45	1.30	1.341	216.78	1870.08	1.61	14.26

3.4. Dielectric properties

The response of dielectric functions was evaluated using the Bethe-Salpeter equation (BSE)²⁹ in accordance with the HSE calculations. The variation of the imaginary dielectric function is shown

in **Figure 5a**, and the real part is shown in **Figure 5b** with respect to the energy. At 2.52 eV for HfSi₂N₄ and 2.49 eV for HfGe₂N₄, the ϵ_i showed their first peak. The phenomena are deducible from the band structures that appear, as both the MLs HfSi₂N₄ and HfGe₂N₄ possess comparable bandgaps having only a difference of 0.14 eV. The second peaks with high magnitude were situated at 2.94 eV for HfSi₂N₄ and 3.03 eV for HfGe₂N₄. At 2.42 eV and 2.38 eV, the ϵ_r showed the first peaks for HfSi₂N₄ and HfGe₂N₄. The absorption spectra exhibited distinct peaks at 2.53 eV and 2.51 eV, corresponding to α values of $1.01 \times 10^5 \text{ cm}^{-1}$ and $0.53 \times 10^5 \text{ cm}^{-1}$ for HfSi₂N₄ and HfGe₂N₄, respectively (**Figure 5c**), and they match with the already reported values in the literature^{14,30}. Secondary peaks with higher magnitude were also found at 3.04 eV for HfSi₂N₄ and 2.96 eV for HfGe₂N₄. The dependence of η with energy is shown in **Figure 5d**, the obtained value of η is about 1.55 and 1.64 for HfSi₂N₄ and HfGe₂N₄ at zero energy, respectively. The first peaks for both HfSi₂N₄ and HfGe₂N₄ are located at energy levels of 2.43 eV and 2.39 eV, whereas the secondary peaks are observed at higher energy levels of 2.98 eV and 2.85 eV for HfSi₂N₄ and HfGe₂N₄. After 10 eV, the η of HfSi₂N₄ and HfGe₂N₄ become nearly identical.

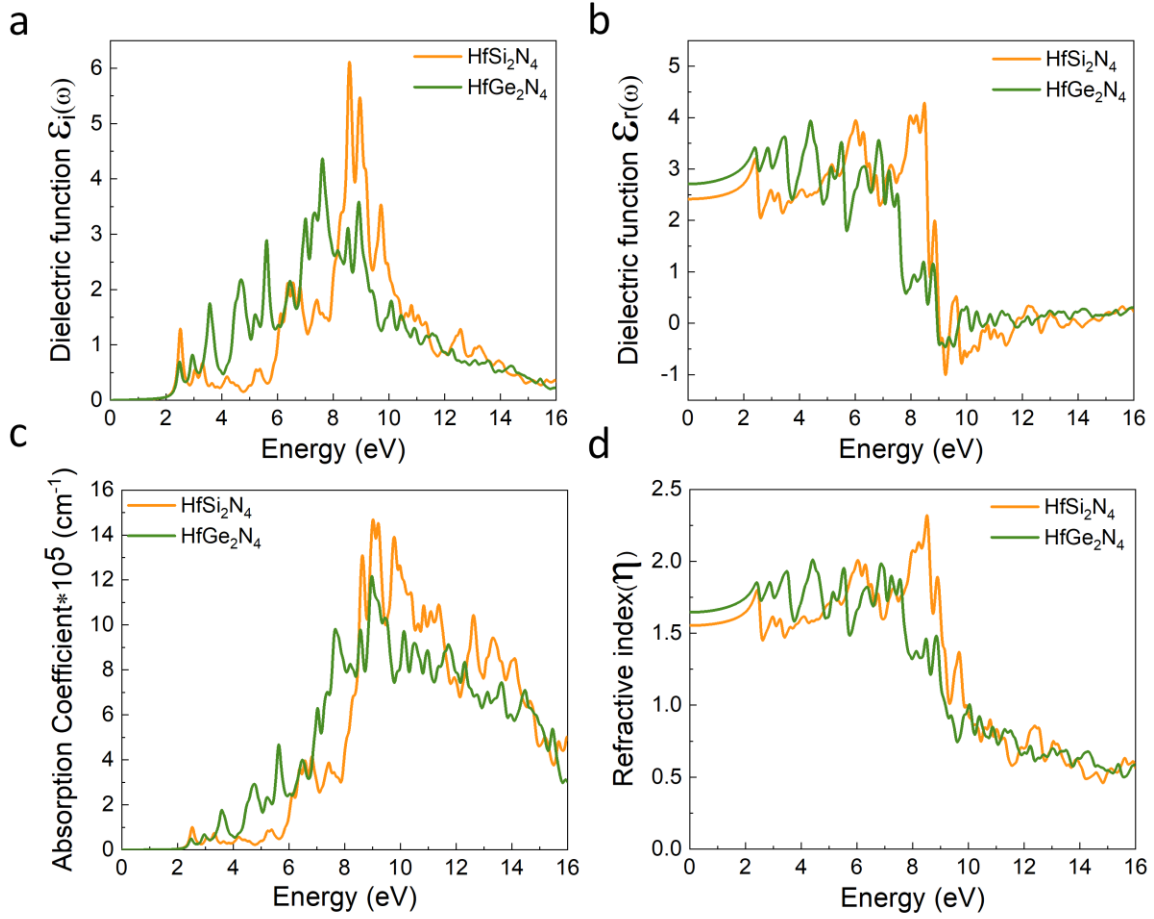


Figure 5: Plot of a) imaginary (ϵ_i), and b) real (ϵ_r) component of the dielectric function, c) absorption coefficient (α), and d) refractive index (η) as a function of energy based on the HSE calculations.

3.5. Thermoelectric Properties

Figure 6a shows the variation of the Seebeck coefficient (S) of the HfSi_2N_4 ML as a function of chemical potential (ϕ) at three specific temperatures: 300 K, 600 K, and 900 K. The highest Seebeck coefficient (S) found for HfSi_2N_4 monolayer (ML) is $-2924.99 \mu\text{VK}^{-1}$ for n-type carriers ($\phi > 0$) and $2994.27 \mu\text{VK}^{-1}$ for p-type carriers ($\phi < 0$) at a temperature of 300 K. The absolute value of S reached its peak at 300 K and subsequently decreases as temperature increases. **Figure 6b** displays the relationship between the relaxation time-scaled electrical conductivity (σ/τ) with respect to ϕ . No significant change was observed in the value of σ/τ with respect to the change in temperature. We observed that the σ/τ for the p-type is lower than that of the n-type in ML

HfSi₂N₄. **Figure 6c** illustrates the relationship between the relaxation time-scaled power factor (PF = $S^2\sigma/\tau$) and ϕ for the HfSi₂N₄ ML. The maximum power factor achieved in a monolayer of HfSi₂N₄ was $38.43 \times 10^{10} \text{ Wm}^{-2}\text{K}^{-1}\text{s}^{-1}$ for p-type carriers ($37.88 \times 10^{10} \text{ Wm}^{-2}\text{K}^{-1}\text{s}^{-1}$ for p-type) at a temperature of 900 K. **Figures 6d, e, and f** illustrate the changes in S , σ/τ , and $S^2\sigma/\tau$ for the HfGe₂N₄ ML as a function of ϕ . The S of the HfSi₂N₄ ML decreases gradually as the temperature increases. The maximum achieved power factor (PF) for the monolayer (ML) of HfGe₂N₄ is $36.87 \times 10^{10} \text{ Wm}^{-2}\text{K}^{-1}\text{s}^{-1}$, specifically for the n-type carriers. The power factor obtained is $13.02 \times 10^{10} \text{ Wm}^{-2}\text{K}^{-1}\text{s}^{-1}$ at a temperature of 900 K for the p-type carriers. The efficiency of n-type doping in HfGe₂N₄ for thermoelectric applications is significantly higher. The Seebeck coefficient (S) of HfSi₂N₄ ML was found to be greater than that of HfGe₂N₄, which can be attributed to the higher bandgap (BG) value of HfSi₂N₄ compared to HfGe₂N₄.

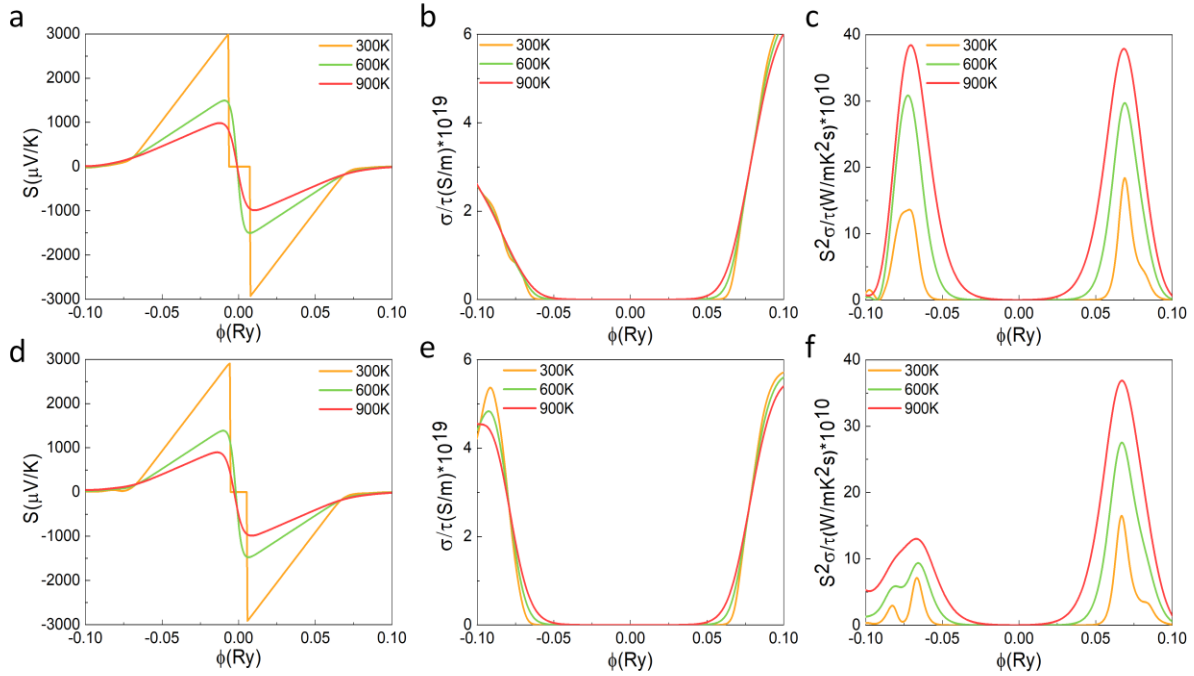


Figure 6: Variation of (a) S (b) σ/τ , and (c) PF for HfSi₂N₄ with respect to ϕ , and variation of (d) S (e) σ/τ , and (f) PF for HfGe₂N₄ with respect to chemical potential ϕ .

3.6. Lattice thermal conductivity (κ_l)

Figures 7a and 7b represent the relationship between the variation of κ_l with temperature for ML of HfSi₂N₄ and HfGe₂N₄. The thermal conductivity (κ_l) of HfGe₂N₄ was found to be significantly

lower ($22.41 \text{ Wm}^{-1}\text{K}^{-1}$) at 300 K compared to HfSi_2N_4 ($38.76 \text{ Wm}^{-1}\text{K}^{-1}$), as well as lower than well-known other 2D TMDCs such as MoS_2 ($34.5 \text{ Wm}^{-1}\text{K}^{-1}$)³¹ and WS_2 ($72 \text{ Wm}^{-1}\text{K}^{-1}$)¹². Both structures exhibit a drop in κ_l as temperature increases. The monolayer (ML) of HfGe_2N_4 demonstrated significantly reduced κ_l compared to the monolayer of WSi_2N_4 , even at elevated temperatures⁹.

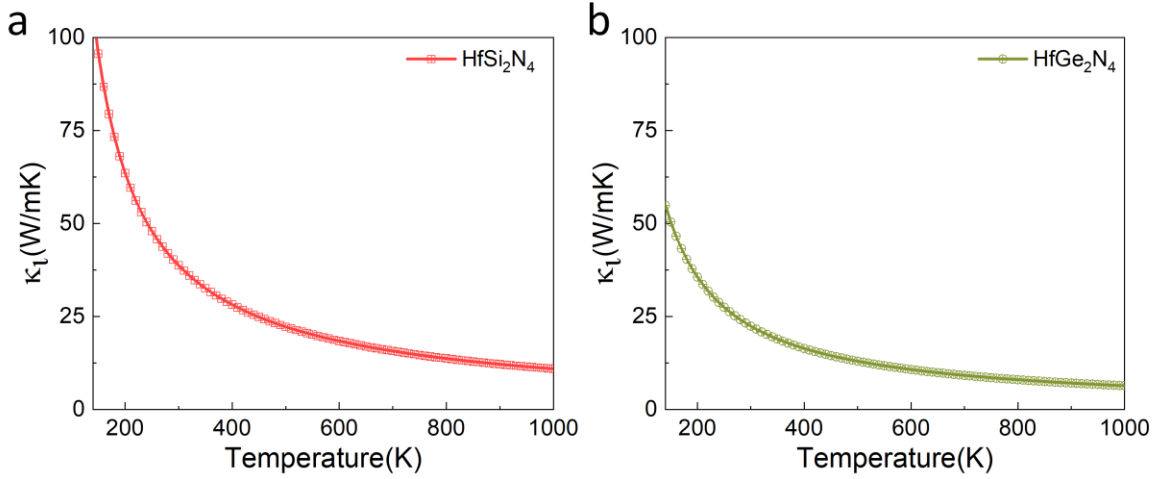


Figure 7: Temperature-dependent variation of κ_l for ML (a) HfSi_2N_4 and (b) HfGe_2N_4 .

Figure 8 shows the variation of group velocity (G_v) and Grüneisen parameters (γ) with respect to frequency for both MLs. The lattice thermal conductivity difference can be found from group velocity analysis. **Figure 8a** shows a maximum G_v of about $11.0 \times 10^3 \text{ m/s}$ for the HfSi_2N_4 ML precisely because of the longitudinal acoustic mode. Similarly, the HfGe_2N_4 ML showed a maximum G_v of about $9.1 \times 10^3 \text{ m/s}$ (**Figure 8b**), which is also specifically because of the longitudinal acoustic mode. Since the value of κ_l is directly proportional to G_v , it is straightforward to explain the difference in values of κ_l for the MLs. Due to the significantly greater G_v value of HfSi_2N_4 ML compared to HfGe_2N_4 , the thermal conductivity (κ_l) is also much higher in HfSi_2N_4 . It was found that the presence of both acoustic mode and optical mode phonon bands are distinct with no overlap by analyzing the phonon dispersion curve of HfSi_2N_4 . Therefore, the acoustic and optical phonon scattering is less probable to occur, which is evident in κ_l values for HfSi_2N_4 and HfGe_2N_4 ML. A decrease in the overall phonon frequencies was found due to the presence of the heavier Ge atom in HfGe_2N_4 when compared to HfSi_2N_4 . In HfGe_2N_4 , there is a simultaneous presence of low-lying optical phonons and acoustic phonons, with some degree of overlap. It has

been observed that low-lying optical phonons are close to acoustic phonons and sometimes overlap in HfGe₂N₄. This leads to enhanced scattering of acoustic phonons by the optical phonons, which is responsible for the lowering value of κ_l for the HfGe₂N₄ ML²⁹. The calculation of the Grüneisen parameter (γ) is also included in our study. Slack's equation states that the κ_l varies inversely to the square of γ ³³, which can be inferred from our analysis. From **Figure 8c and d** we can see that the HfGe₂N₄ possessed a higher (anharmonicity) value (γ) compared to HfSi₂N₄, which follows the same trend of κ_l i.e., HfSi₂N₄ possesses higher value of κ_l compared to HfGe₂N₄

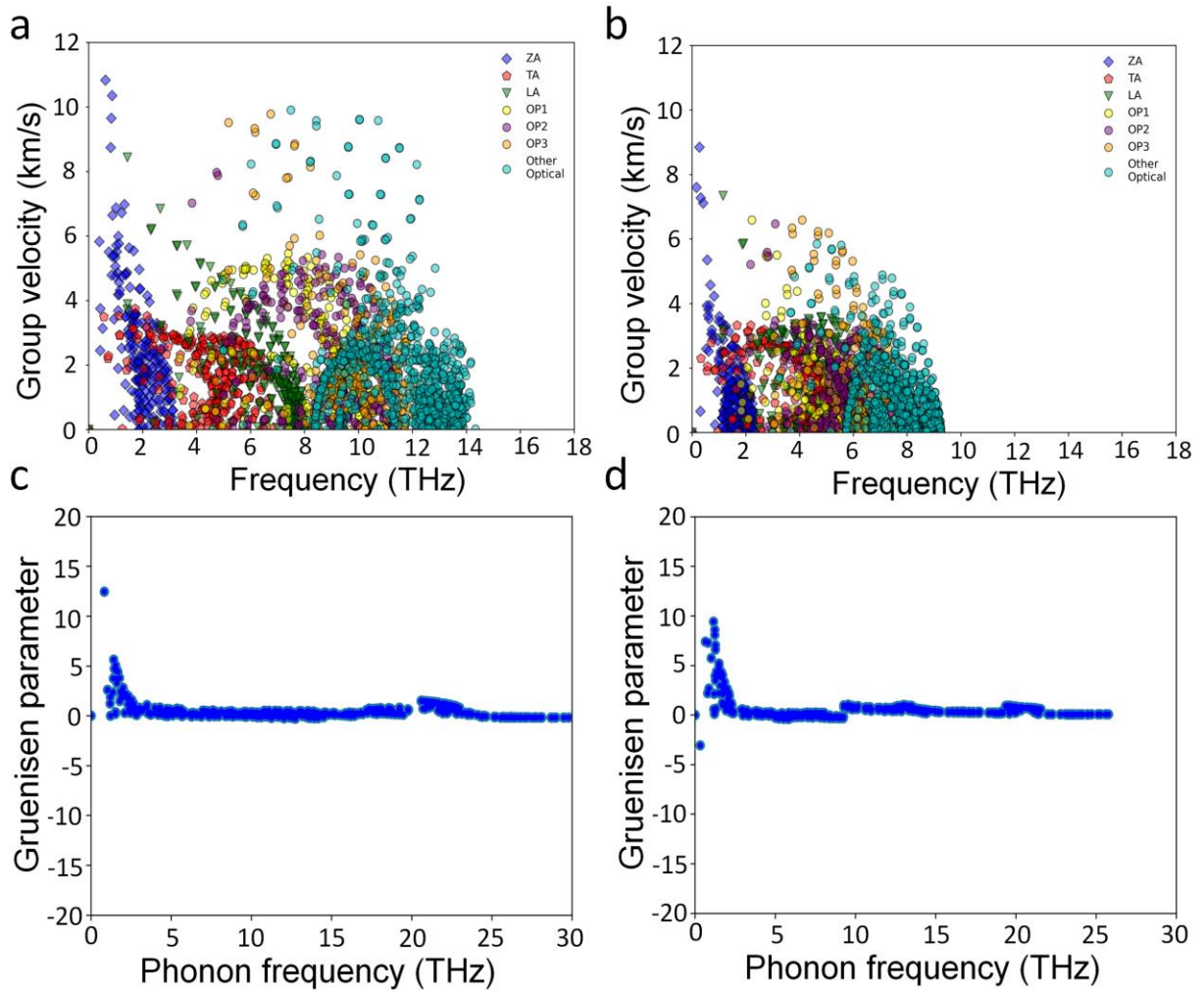


Figure 8: Representation of G_v for different modes with respect to the frequency for (a) HfSi₂N₄ and (b) HfGe₂N₄ ML. Variation of Grüneisen parameters (γ) with phonon frequency for (c) HfSi₂N₄ and (d) HfGe₂N₄ MLs

3.7. Figure of merit (ZT)

A high ZT value requires a high value of S and σ and a considerably lower value of k ($k_e + k_l$), as indicated in the equation 8. The figure of merit (ZT) is defined as

$$ZT = \frac{S^2 \sigma T}{\kappa_e + \kappa_l}, \quad (8)$$

where S is the Seebeck coefficient, T is the temperature, σ is the electrical conductivity, and κ_e and κ_l are the components of thermal conductivity, as stated earlier. **Figure 9 (a) and (b)** show the relation between the ZT and ϕ for the ML of HfSi_2N_4 and HfGe_2N_4 , respectively, at different temperatures. HfGe_2N_4 ML shows a higher ZT value at 900 K compared to HfSi_2N_4 , i.e., 0.90 and 0.83 for p-type and n-type doping, respectively. Additionally, at 900 K, the HfSi_2N_4 ML demonstrated a significant ZT of 0.89 for the p-type and 0.79 for the n-type. The p-type doping exhibited greater ZT values in comparison to the doping with n-type for both structures. The ZT values obtained from the HfSi_2N_4 and HfGe_2N_4 at different temperatures are shown in **Table 3**.

Table 3: Obtained ZT at different temperatures of ML of HfSi_2N_4 and HfGe_2N_4 .

Temperature K	ZT			
	HfSi_2N_4		HfGe_2N_4	
	p	n	p	n
300	0.55	0.32	0.68	0.41
600	0.82	0.66	0.84	0.73
900	0.89	0.79	0.90	0.83

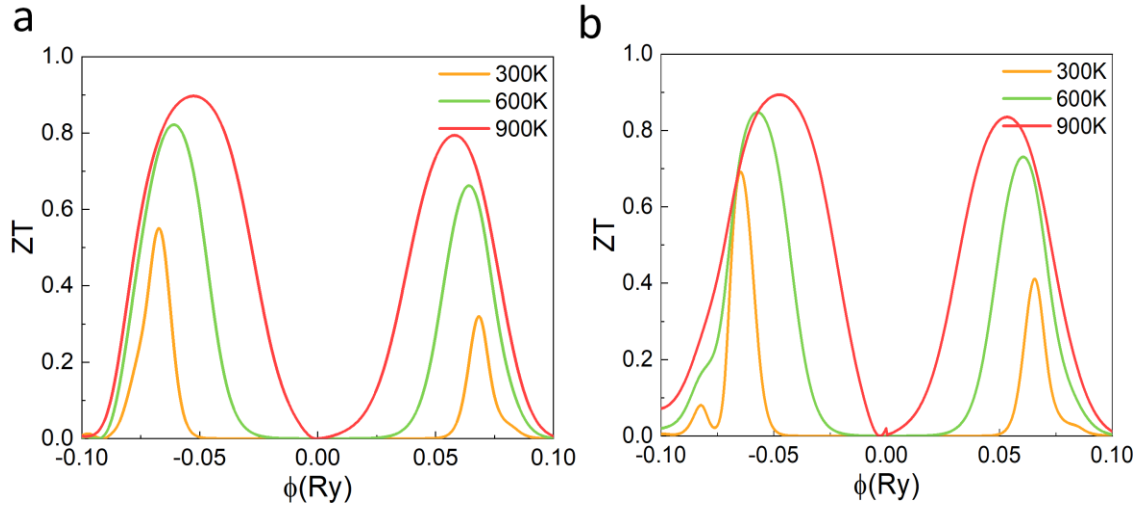


Figure 9: Representation of ZT for different temperatures (T) as a function of ϕ for (a) HfSi_2N_4 and (b) HfGe_2N_4 ML.

4. Conclusions

We studied optoelectronic and thermoelectric properties using first-principles calculations. The structural stability for both the MLs was verified from the phonon dispersion relations which are free from imaginary frequencies. The ZT for both HfSi_2N_4 and HfGe_2N_4 can be considered very good for thermoelectric applications for both low-temperature and high-temperature thermoelectric devices in the future. The HfGe_2N_4 showed a better k_l value compared to many popular TMDCs. The HfGe_2N_4 showed ZT values of 0.68, 0.84, and 0.90 at room temperature (300 K), 600 K, and 900 K for p-doping. So, here, p-doping is more effective than n-doping. The S and σ of HfSi_2N_4 is more significant rather than HfGe_2N_4 , so the PF of HfSi_2N_4 is higher than HfGe_2N_4 , But the k_l of HfGe_2N_4 is found to be lower than HfSi_2N_4 so the ZT of HfGe_2N_4 become higher. The HfGe_2N_4 ML can also be used as a low-temperature thermoelectric device as it showed considerable ZT at room temperature.

Acknowledgments:

We are thankful to the INSPIRE program and the Indian Institute of Technology Jodhpur for their financial assistance and necessary facilities to conduct the research.

Reference:

- 1 G. Eda, T. Fujita, H. Yamaguchi, D. Voiry, M. Chen and M. Chhowalla, Coherent atomic and electronic heterostructures of single-layer MoS₂, *ACS Nano*, 2012, **6**, 7311–7317.
- 2 S. Karak, J. Bera, S. Paul, S. Sahu and S. Saha, Low thermal conductivity and interface thermal conductance in SnS_2 , *Phys. Rev. B*, 2021, **104**, 195304.
- 3 Z.-L. Lei and B. Guo, 2D Material-Based Optical Biosensor: Status and Prospect, *Adv. Sci.*, 2022, **9**, 2102924.
- 4 X. Cai, Y. Luo, B. Liu and H.-M. Cheng, Preparation of 2D material dispersions and their applications, *Chem. Soc. Rev.*, 2018, **47**, 6224–6266.
- 5 M. Long, P. Wang, H. Fang and W. Hu, Progress, Challenges, and Opportunities for 2D Material Based Photodetectors, *Adv. Funct. Mater.*, 2019, **29**, 1803807.
- 6 Z. Guan, H. Hu, X. Shen, P. Xiang, N. Zhong, J. Chu and C. Duan, Recent Progress in Two-Dimensional Ferroelectric Materials, *Adv. Electron. Mater.*, 2020, **6**, 1900818.
- 7 Y.-L. Hong, Z. Liu, L. Wang, T. Zhou, W. Ma, C. Xu, S. Feng, L. Chen, M.-L. Chen, D.-M. Sun, X.-Q. Chen, H.-M. Cheng and W. Ren, Chemical vapor deposition of layered two-dimensional MoSi₂N₄ materials, *Science (80-.)*, 2020, **369**, 670–674.
- 8 B. Mortazavi, B. Javvaji, F. Shojaei, T. Rabczuk, A. V Shapeev and X. Zhuang, Exceptional piezoelectricity, high thermal conductivity and stiffness and promising photocatalysis in two-dimensional MoSi₂N₄ family confirmed by first-principles, *Nano Energy*, 2021, **82**, 105716.
- 9 C. Das, M. Alam, D. Saikia, A. Betal, A. N. Gandhi and S. Sahu, A Strategic Comparison Between Monolayers of WX₂N₄(X≐Si, Ge) Toward Thermoelectric Performance and Optoelectronic Properties., *Adv. Theory Simulations*, 2023, **n/a**, 2300981.
- 10 Q. Tan, L.-D. Zhao, J.-F. Li, C.-F. Wu, T.-R. Wei, Z.-B. Xing and M. G. Kanatzidis, Thermoelectrics with earth abundant elements: low thermal conductivity and high

- thermopower in doped SnS, *J. Mater. Chem. A*, 2014, **2**, 17302–17306.
- 11 M. Beaumale, T. Barbier, Y. Bréard, G. Guelou, A. V Powell, P. Vaquero and E. Guilmeau, Electron doping and phonon scattering in $Ti_{1+x}S_2$ thermoelectric compounds, *Acta Mater.*, 2014, **78**, 86–92.
 - 12 J. Bera and S. Sahu, Strain induced valley degeneracy: a route to the enhancement of thermoelectric properties of monolayer WS₂, *RSC Adv.*, 2019, **9**, 25216–25224.
 - 13 J. Bera, A. Betal and S. Sahu, Spin orbit coupling induced enhancement of thermoelectric performance of HfX₂ (X= S, Se) and its Janus monolayer, *J. Alloys Compd.*, 2021, **872**, 159704.
 - 14 C. Das, A. Betal, M. Alam, J. Bera, A. N. Gandhi and S. Sahu, Thermoelectric performance and optoelectronic properties of Janus monolayer of ZrXY (X= O, S)(Y= S, Se), *Comput. Mater. Sci.*, 2023, **218**, 111993.
 - 15 C. Zhang, F. Wei, X. Zhang, W. Chen, C. Chen, J. Hao and B. Jia, Thermoelectric properties of monolayer MoSi₂N₄ and MoGe₂N₄ with large Seebeck coefficient and high carrier mobility: A first principles study, *J. Solid State Chem.*, 2022, **315**, 123447.
 - 16 G. Kresse and J. Furthmüller, Efficient iterative schemes for ab initio total-energy calculations using a plane-wave basis set, *Phys. Rev. B*, 1996, **54**, 11169.
 - 17 P. E. Blöchl, Projector augmented-wave method, *Phys. Rev. B*, 1994, **50**, 17953.
 - 18 G. Kresse and D. Joubert, From ultrasoft pseudopotentials to the projector augmented-wave method, *Phys. Rev. b*, 1999, **59**, 1758.
 - 19 J. P. Perdew, K. Burke and M. Ernzerhof, Generalized gradient approximation made simple, *Phys. Rev. Lett.*, 1996, **77**, 3865.
 - 20 J. Heyd, G. E. Scuseria and M. Ernzerhof, Hybrid functionals based on a screened Coulomb potential, *J. Chem. Phys.*, 2003, **118**, 8207–8215.
 - 21 P. Giannozzi, O. Barone, P. Bonfà, D. Brunato, R. Car, I. Carnimeo, C. Cavazzoni, S. De Gironcoli, P. Delugas and F. Ferrari Ruffino, Quantum ESPRESSO toward the exascale, *J. Chem. Phys.*

- 22 P. Giannozzi, S. Baroni, N. Bonini, M. Calandra, R. Car, C. Cavazzoni, D. Ceresoli, G. L. Chiarotti, M. Cococcioni and I. Dabo, QUANTUM ESPRESSO: a modular and open-source software project for quantum simulations of materials, *J. Phys. Condens. matter*, 2009, **21**, 395502.
- 23 G. K. H. Madsen and D. J. Singh, BoltzTraP. A code for calculating band-structure dependent quantities, *Comput. Phys. Commun.*, 2006, **175**, 67–71.
- 24 A. Yadav, J. Kangsabanik, N. Singh and A. Alam, Novel two-dimensional MA₂N₄ materials for photovoltaic and spintronic applications, *J. Phys. Chem. Lett.*, 2021, **12**, 10120–10127.
- 25 J. Bardeen and W. Shockley, Deformation potentials and mobilities in non-polar crystals, *Phys. Rev.*, 1950, **80**, 72.
- 26 M. Pei, X. Zhao, C. Xia, T. Wang, X. Dai and S. Wei, Tuning the band alignment and electronic properties of XSe₂/WSi₂N₄ (X= Mo, W) van der waals heterostructures with high carrier mobility, *Phys. E Low-dimensional Syst. Nanostructures*, 2023, **149**, 115656.
- 27 A. Rawat, N. Jena, D. Dimple and A. De, Sarkar, A comprehensive study on carrier mobility and artificial photosynthetic properties in group VI B transition metal dichalcogenide monolayers, *J. Mater. Chem. A*, 2018, **6**, 8693–8704.
- 28 S. H. Mir, V. K. Yadav and J. K. Singh, Recent Advances in the Carrier Mobility of Two-Dimensional Materials: A Theoretical Perspective, *ACS Omega*, 2020, **5**, 14203–14211.
- 29 E. E. Salpeter and H. A. Bethe, A relativistic equation for bound-state problems, *Phys. Rev.*, 1951, **84**, 1232.
- 30 A. Betal, J. Bera and S. Sahu, Low-temperature thermoelectric behavior and impressive optoelectronic properties of two-dimensional XI₂ (X= Sn, Si): A first principle study, *Comput. Mater. Sci.*, 2021, **186**, 109977.
- 31 R. Yan, J. R. Simpson, S. Bertolazzi, J. Brivio, M. Watson, X. Wu, A. Kis, T. Luo, A. R. Hight Walker and H. G. Xing, Thermal conductivity of monolayer molybdenum disulfide obtained from temperature-dependent Raman spectroscopy, *ACS Nano*, 2014, **8**, 986–993.

- 32 L. Zhang, X. Chen, D. Guo, G. Zhu, J. Li, X. Meng and F. Zhai, Ultralow lattice thermal conductivity and promising thermoelectric properties of a new 2D MoW₃Te₈ membrane, *Results Phys.*, 2023, **44**, 106136.
- 33 G. A. Slack, Nonmetallic crystals with high thermal conductivity, *J. Phys. Chem. Solids*, 1973, **34**, 321–335.